

Banner appropriate to article type will appear here in typeset article

Energy pathways in large- and small-scale convection-driven dynamos.

Souvik Naskar¹, Anikesh Pal¹†

¹Department of Mechanical Engineering, Indian Institute of Technology, Kanpur 208016, India

(Received xx; revised xx; accepted xx)

We investigate the energy pathways between the velocity and the magnetic fields in a rotating plane layer dynamo driven by Rayleigh-Bénard convection using direct numerical simulations. The kinetic and magnetic energies are divided into mean and turbulent components to study the production, transport, and dissipation associated with large and small-scale dynamos. This energy balance-based characterization reveals distinct mechanisms for large- and small-scale magnetic field generation in dynamos, depending on the nature of the velocity field and the conditions imposed at the boundaries.

Key words:

1. Introduction

Hydromagnetic dynamo action is the commonly accepted source of magnetic fields in planets and stars. We explore the energy balance in a plane layer convection-driven Childress-Soward (CS) dynamo (Childress & Soward 1972). In this simple Cartesian dynamo model, driven by rotating Rayleigh-Bénard convection (RBC), the velocity field provides energy to the magnetic field to sustain the dynamo action against Joule dissipation. Our analysis distinguishes between the part of the kinetic energy that produces the horizontally-averaged large-scale mean magnetic field and the small-scale turbulent magnetic field. Based on this decomposition, we derive the kinetic and magnetic energy budgets and characterize a dynamo with both large- and small-scale magnetic fields in terms of their energy conversion mechanisms.

Dynamos are generally classified based on the scale of the magnetic field generated by them Brandenburg & Subramanian (2005). The magnetic field for a large-scale dynamo has a length scale larger than the velocity field, whereas the length scale of the magnetic field is smaller than the velocity field for a small-scale dynamo. For a plane layer dynamo, this classification is apparent from the fraction of energy in the mean magnetic field to the total magnetic energy (Tilgner 2012). The magnetic Reynolds number at the convective scale \widetilde{Rm} , representing the dominance of electromagnetic induction over ohmic diffusion, is one of the

† Email address for correspondence: pala@iitk.ac.in

important diagnostic quantities that decides this mean energy fraction. Large-scale dynamos with high mean energy fraction, $O(0.1)$ has been found to operate at low magnetic Reynolds numbers $\widetilde{Rm} \lesssim 13$ (Tilgner 2012), where kinetic helicity has been proposed as a driving mechanism. Conversely, higher values of \widetilde{Rm} lead to small-scale magnetic field generation driven by the stretching of magnetic field lines by the velocity field, with comparatively lower mean energy fraction. However, a recent study Yan & Calkins (2022) demonstrates the existence of large-scale dynamos, despite the presence of a strongly turbulent velocity field with low helicity. In the present investigation, we use the kinetic and magnetic energy budgets to understand the various mechanisms associated with large-and small-scale magnetic field generation.

2. Method

2.1. Governing Equations

In this study, the CS dynamo is driven by a classical Rayleigh-Bénard convection setup with a plane layer of incompressible, electrically conducting, Boussinesq fluid kept between two parallel plates with a distance d and temperature difference ΔT , where the lower plate is hotter than the upper plate. The system rotates with a constant angular velocity Ω about the vertical axis, anti-parallel to the gravity g . This fluid has the kinematic viscosity ν , thermal diffusivity κ , adiabatic volume expansion coefficient α , and magnetic diffusivity η . The Navier-Stokes equations, coupled with the energy equation, the Maxwell equation, and the solenoidal field conditions, govern the velocity, pressure, temperature, and the magnetic field $\{u_i, p, \theta, B_i\}$ (Naskar & Pal 2022a,b) as presented below.

$$\frac{\partial u_j}{\partial x_j} = \frac{\partial B_j}{\partial x_j} = 0, \quad (2.1)$$

$$\frac{\partial u_i}{\partial t} + u_j \frac{\partial u_i}{\partial x_j} = -\frac{\partial p}{\partial x_i} + \frac{1}{E} \sqrt{\frac{Pr}{Ra}} \epsilon_{ij3} u_j \hat{e}_3 + B_j \frac{\partial B_i}{\partial x_j} + \theta \delta_{i3} + \sqrt{\frac{Pr}{Ra}} \frac{\partial^2 u_i}{\partial x_j \partial x_j}, \quad (2.2)$$

$$\frac{\partial \theta}{\partial t} + u_j \frac{\partial \theta}{\partial x_j} = \frac{1}{\sqrt{RaPr}} \frac{\partial^2 \theta}{\partial x_j \partial x_j}, \quad (2.3)$$

$$\frac{\partial B_i}{\partial t} + u_j \frac{\partial B_i}{\partial x_j} = B_j \frac{\partial u_i}{\partial x_j} + \sqrt{\frac{Pr}{Ra}} \frac{1}{Pr_m} \frac{\partial^2 B_i}{\partial x_j \partial x_j}. \quad (2.4)$$

The governing non-dimensional parameters are the Rayleigh number ($Ra = g\alpha\Delta T d^3 / \kappa\nu$) and Ekman number ($E = \nu / 2\Omega d^2$) representing the thermal forcing and rotation rates, respectively, whereas, the thermal and magnetic Prandtl numbers ($Pr = \nu / \kappa$ and $Pm = \nu / \eta$) are the properties of the fluid. The current setup is a local approximation to the astrophysically more relevant spherical shell dynamo models (Tilgner 2012). In the horizontal directions (x_1, x_2) periodic boundary conditions are applied. Both no-slip and free-slip boundary conditions have been used in the vertical direction (x_3).

$$\begin{aligned} u_1 = u_2 = u_3 = 0 \quad \text{at } x_3 = \pm 1/2 \quad (\text{no-slip}) \\ \frac{\partial u_1}{\partial x_3} = \frac{\partial u_2}{\partial x_3} = 0, \quad u_3 = 0 \quad \text{at } x_3 = \pm 1/2 \quad (\text{free-slip}). \end{aligned} \quad (2.5)$$

Thermal boundary conditions are isothermal with unstable temperature gradients.

$$\theta = 1/2 \text{ at } x_3 = -1/2, \quad \theta = -1/2 \text{ at } x_3 = 1/2 \quad (2.6)$$

Perfectly conducting and pseudo-vacuum boundary conditions have been used for the magnetic field.

$$\begin{aligned} \frac{\partial B_1}{\partial x_3} = \frac{\partial B_2}{\partial x_3} = B_3 = 0 \text{ at } x_3 = \pm 1/2 & \quad (\text{perfectly conducting}) \\ B_1 = B_2 = \frac{\partial B_3}{\partial x_3} = 0 \text{ at } x_3 = \pm 1/2 & \quad (\text{pseudo-vacuum}) \end{aligned} \quad (2.7)$$

2.2. Energy Budget

We perform a Reynolds decomposition of the variables into mean and fluctuating parts such that $\phi(x, y, z, t) = \bar{\phi}(z, t) + \phi'(x, y, z, t)$ where $\phi = \{u_i, p, \theta, B_i\}$. Here, the over-bar denotes an average over the horizontal directions (Tilgner 2012; Naskar & Pal 2022b). The kinetic energy ($K = 1/2 u_i u_i$) and magnetic energy ($M = 1/2 B_i B_i$) are also divided into the mean (\mathfrak{K} and \mathfrak{M}) and turbulent (\mathcal{K} and \mathcal{M}) components, and are presented in equations 2.8-2.11. These equations can be derived in three steps: (1) horizontally averaging equations 2.2 and 2.4 to get the mean momentum and mean Maxwell equations respectively, and then subtracting these mean equations from 2.2 and 2.4 to get the fluctuating parts of momentum and Maxwell equations (2) multiplying the mean velocity and mean magnetic field with mean momentum and mean Maxwell equations respectively, to get evolution equations for \mathfrak{K} and \mathfrak{M} , (3) multiplying the fluctuating velocity and magnetic fields with fluctuating parts of momentum and Maxwell equations respectively, and averaging them to get evolution equations for \mathcal{K} and \mathcal{M} . This decomposition into mean and turbulent parts of the energies is the primary distinctive feature of the present study from an earlier budget analysis of a dynamo (Brandenburg *et al.* 1996). The turbulent kinetic energy (TKE) (Naskar & Pal 2022b) evolves as:

$$d\mathcal{K}/dt = \mathcal{S} + \mathcal{B} - \mathcal{D} - \partial \mathcal{T}_j / \partial x_j + \mathcal{P}, \quad (2.8)$$

where $\mathcal{K} = 1/2 \overline{u'_i u'_i}$ is the TKE, $\mathcal{S} = -\overline{u'_i u'_j} \partial \bar{u}_i / \partial x_j$ is the production of TKE by mean shear, $\mathcal{B} = \overline{u'_3 \theta'}$ is the conversion of available potential energy (APE) to TKE by the turbulent buoyancy flux (Gayen *et al.* 2013), $\mathcal{D} = \sqrt{Pr/Ra} \overline{\partial u'_i / \partial x_j \partial u'_i / \partial x_j}$ is the viscous dissipation which converts TKE to internal energy (IE), $\partial \mathcal{T}_j / \partial x_j$ is the redistribution of TKE (Petschel *et al.* 2015), representing the divergence of the TKE flux $\mathcal{T}_j = \mathcal{T}_p + \mathcal{T}_t + \mathcal{T}_v + \mathcal{T}_M$. The components of the TKE flux are the pressure flux, $\mathcal{T}_p = \overline{u'_j p'}$, the turbulent flux $\mathcal{T}_t = \frac{1}{2} \overline{u'_i u'_i u'_j}$, the viscous flux $\mathcal{T}_v = -\sqrt{Pr/Ra} \partial \mathcal{K} / \partial x_j$, and the magnetic flux $\mathcal{T}_M = -\overline{B_j u'_i B'_i} - \overline{u'_i B'_i B'_j}$.

In equation 2.8, the term \mathcal{P} represents the production of \mathcal{K} due to work done by the Lorentz force on the flow field. It can be further divided into three components $\mathcal{P} = -\mathcal{P}_1 + \mathcal{P}_2 - \mathcal{P}_3$, where $\mathcal{P}_1 = \overline{B_j B'_i \partial u'_i / \partial x_j}$ is the production of TME from TKE due to work done by the fluctuating strain rate on the mean magnetic field, $\mathcal{P}_2 = \overline{u'_i B'_j \partial \bar{B}_i / \partial x_j}$ signifies the production of TKE due to mean magnetic field gradient and $\mathcal{P}_3 = \overline{B'_i B'_j \partial u'_i / \partial x_j}$ represents the amplification (or attenuation) of the magnetic energy, due to work done by stretching (or squeezing) of small-scale magnetic field lines by the fluctuating velocity gradients.

The mean kinetic energy (MKE) budget is expressed as,

$$d\mathfrak{K}/dt = -\mathcal{S} + \mathfrak{B} - \mathfrak{D} - \partial \mathfrak{T}_j / \partial x_j + \mathfrak{P} \quad (2.9)$$

where $\mathfrak{K} = 1/2\bar{u}_i\bar{u}_i$ is the MKE, $\mathfrak{B} = \bar{u}_3\bar{\theta}$ is the mean buoyancy flux, $\mathfrak{D} = \sqrt{Pr/Ra}\partial\bar{u}_i/\partial x_j\partial\bar{u}_i/\partial x_j$ is the mean viscous dissipation, and $\partial\mathfrak{Z}_j/\partial x_j$ is the divergence of the MKE flux $\mathfrak{Z}_j = \bar{u}_j\bar{p} + 1/2\overline{u'_i u'_j \bar{u}_i} - \sqrt{Pr/Ra}\partial\mathfrak{K}/\partial x_j - \overline{B'_i B'_j \bar{u}_i} - \bar{B}_i \bar{B}_j \bar{u}_i$. Here $\mathfrak{P} = -\mathcal{P}_4 - \mathcal{P}_5$, where, $\mathcal{P}_4 = \overline{B'_i B'_j \partial\bar{u}_i/\partial x_j}$ represents the work done by the mean shear on the fluctuating component of the magnetic fields whereas, the work done on the mean component of the magnetic fields is represented by $\mathcal{P}_5 = \bar{B}_i \bar{B}_j \partial\bar{u}_i/\partial x_j$.

The equations for the evolution of the turbulent and the mean magnetic energies are presented below. As the Maxwell equation (Naskar & Pal 2022a,b) is similar to the vorticity transport equation, the magnetic energy equations resemble enstrophy transport equations (Lumley & Tennekes 1997). The turbulent magnetic energy (TME) budget equation is given below.

$$d\mathcal{M}/dt = -\mathcal{D}^M - \partial\mathcal{T}_j^M/\partial x_j + \mathcal{P}^M \quad (2.10)$$

where, $\mathcal{M} = 1/2\overline{B'_i B'_i}$ is the TME, $\mathcal{D}^M = 1/Pm\sqrt{Pr/Ra} \overline{\partial B'_i/\partial x_j \partial B'_i/\partial x_j}$ is the Joule dissipation, $\partial\mathcal{T}_j^M/\partial x_j$ is the redistribution of TME flux given by $\mathcal{T}_j^M = 1/2\overline{B'_i B'_i u'_j} - 1/Pm\sqrt{Pr/Ra}\partial\mathcal{M}/\partial x_j$. Here, the energy exchange terms can be expressed as $\mathcal{P}^M = \mathcal{P}_1 + \mathcal{P}_3 + \mathcal{P}_4 - \mathcal{P}_6$, where $\mathcal{P}_6 = \overline{u'_j B'_i \partial B'_i/\partial x_j}$ exchange energy between the turbulent and mean magnetic fields. We can anticipate its appearance in the mean magnetic energy (MME) equations with an opposite sign.

$$d\mathfrak{M}/dt = -\mathfrak{D}^M - \partial\mathfrak{Z}_j^M/\partial x_j + \mathfrak{P}^M \quad (2.11)$$

where, $\mathfrak{M} = 1/2\bar{B}_i\bar{B}_i$ is the MME, $\mathfrak{D}^M = 1/Pm\sqrt{Pr/Ra}\partial\bar{B}_i/\partial x_j\partial\bar{B}_i/\partial x_j$ is the mean Joule dissipation, and $\partial\mathfrak{Z}_j^M/\partial x_j$ is the divergence of MME flux $\mathfrak{Z}_j^M = \bar{B}_i \overline{u'_j B'_i} - \bar{B}_i \overline{u'_i B'_j} - 1/Pm\sqrt{Pr/Ra}\frac{\partial\mathfrak{M}}{\partial x_j}$. Energy exchange terms in the MME equation can be expressed as $\mathfrak{P}^M = -\mathcal{P}_2 + \mathcal{P}_5 + \mathcal{P}_6$.

We plot an energy pathway diagram by averaging the terms in the energy budget equations in the vertical direction to obtain the volume averaged quantities, as shown in figure 1. The transport terms become negligible due to this volume-averaging, and we can demonstrate the conversion paths between KE and ME sustaining the dynamo action. The APE is converted to MKE and TKE via the mean and turbulent part of the buoyancy flux (Gayen *et al.* 2013) respectively. The shear production term, \mathcal{S} , may also produce TKE in the presence of a mean shear. The small-scale turbulent flow can exchange energy with the small-scale magnetic field through \mathcal{P}_1 or \mathcal{P}_3 or both, or with the large-scale mean magnetic field through \mathcal{P}_2 . The large-scale flow can exchange energy with the small-scale and large-scale magnetic field through \mathcal{P}_4 and \mathcal{P}_5 , respectively. The term \mathcal{P}_6 may produce TME by extracting energy from the mean magnetic field. It may also produce MME by transferring energy from the turbulent magnetic field to the mean magnetic field. Finally, the viscous dissipation components (\mathfrak{D} and \mathcal{D}) convert KE to IE, while the ME is transformed to IE via Joule dissipation components (\mathfrak{D}^M and \mathcal{D}^M). In the absence of a horizontally-averaged mean velocity field, as in the present problem, the energy pathways associated with MKE, marked in grey, are insignificant.

2.3. Numerical Details

To characterize the different types of dynamos based on the energy pathway diagram in figure 1, we perform DNS of RBC-driven dynamos in a doubly-periodic domain of unit aspect ratio. We use 1024 uniform grids in each horizontal direction (x_1 and x_2) and 256 grids in the vertical direction (x_3) that are clustered near the boundaries. A finite-difference solver has been used for the simulations that have been validated extensively for studies on

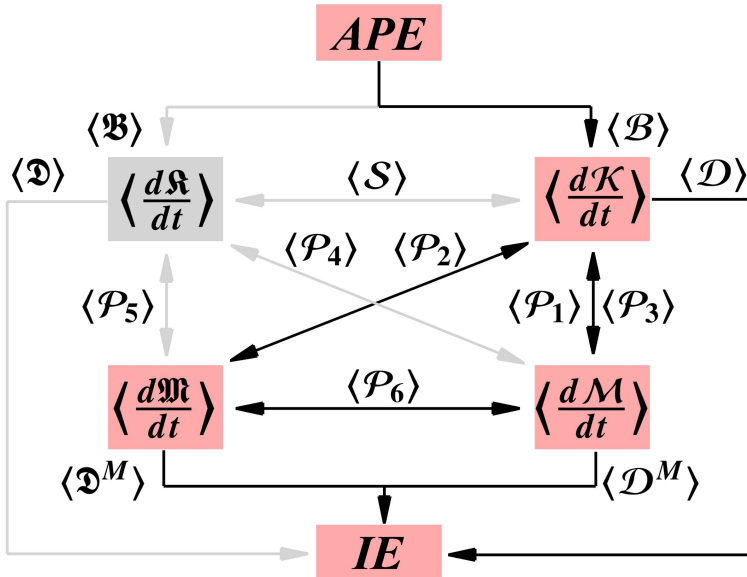


Figure 1: Energy pathways between the kinetic and magnetic energies in a convection-driven dynamo. The energetic terms shown here are volume-averaged as indicated by angular brackets $\langle \cdot \rangle$. The energy pathways marked in grey are negligible in the absence of a mean flow.

case	\mathcal{R}	Pm	Ro_C	\widetilde{Ra}	\widetilde{Rm}	$\langle \mathfrak{M} \rangle / M$	M/E	Nu	type
R10Pm1N	10	1	0.069	76.0	33.4	0.0006	0.1749	55.0	small
R10Pm1F	10	1	0.074	87.0	25.9	0.0097	0.9350	64.7	small
R10Pm0.1F	10	0.1	0.074	87.0	3.2	0.2811	0.7605	60.7	large
R2Pm0.2N	2	0.2	0.031	15.2	1.5	0.6129	0.4866	8.5	large

Table 1: Volume-averaged diagnostic quantities for the dynamo simulations at $E = 5 \times 10^{-7}$ and $Pr = 1$. The last column indicates the dynamo types.

rotating stratified flow (Pal & Chalamalla 2020), and various transitional and turbulent shear flows (Pal *et al.* 2013; Pal & Sarkar 2015; Pal 2020). Details of the solver, the validation studies, the rationale behind the choice of the grids, and the domain size are given in (Naskar & Pal 2022a,b). We choose two dynamos at $\mathcal{R} = Ra/Ra_c = 10$ and $Pm = 1$ where Ra_c is the Rayleigh number at the onset of non-magnetic rotating convection at $E = 5 \times 10^{-7}$ (Naskar & Pal 2022b). At this Ekman number, the critical Rayleigh number has the value $Ra_c = 3.830 \times 10^9$ for no-slip and $Ra_c = 2.192 \times 10^9$ for free-slip boundary conditions. In table 1, the case R10Pm1N is simulated using no-slip and electrically conducting boundaries, whereas free-slip and pseudo-vacuum boundaries (Naskar & Pal 2022b) are incorporated for the R10Pm1F case. The instantaneous snapshots of the magnetic field in the x_1 -direction, as depicted in figures 2a and b, illustrate the small-scale nature of the magnetic field produced by these turbulent dynamos. Another turbulent dynamo case has been simulated, by lowering Pm to 0.1, following (Yan & Calkins 2022), as denoted by R10Pm0.1F in table 1. In this case, lowering Pm leads to large-scale magnetic field generation, as evident from figure 2c. Additionally, we simulate a case with $\mathcal{R} = 2$ and $Pm = 0.2$ and designate it as R2Pm0.2N.

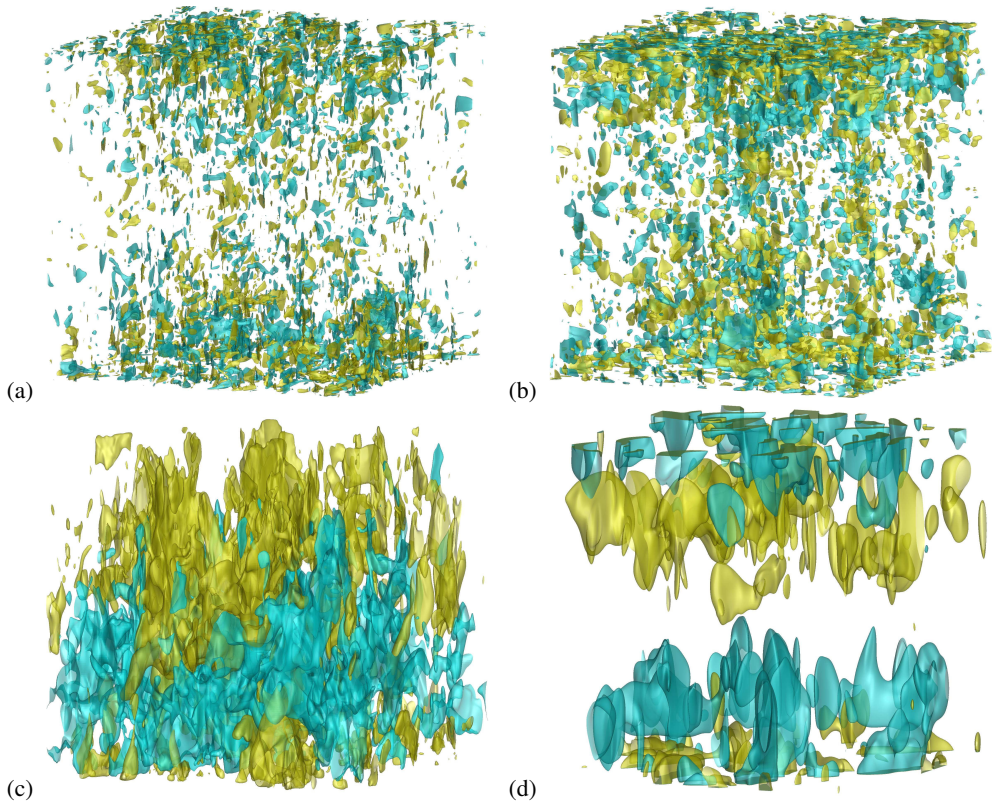


Figure 2: The structure of the magnetic field generated by the dynamos for the cases (a) R10Pm1F, (b) R10Pm1N, (c) R10Pm0.1F, (d) R2Pm0.2N as visualized by the isosurface $B_1 = \pm 0.03$ (olive-positive, blue-negative)

This case is also a large-scale dynamo with weakly-nonlinear convection (Stellmach & Hansen 2004) as demonstrated by the large-scale magnetic field in figure 2d.

The volume-averaged diagnostic parameters reported in table 1 outline the global behaviour of these dynamos. The convective Rossby number, $Ro_C = E(Ra/Pr)^{1/2}$, representing the ratio of inertia to Coriolis force, is of the order 10^{-2} , indicating the dominant role of the Coriolis force. Therefore, all the dynamos are produced by rapidly rotating convection with comparatively small inertia (Naskar & Pal 2022b). The reduced Rayleigh number $\widetilde{Ra} = RaE^{4/3}$ indicates that the dynamos operate in a turbulent state of the flow for $\mathcal{R} = 10$, whereas weakly-nonlinear columnar convection can be observed for $\mathcal{R} = 2$ (Naskar & Pal 2022a; Stellmach & Hansen 2004). The reduced magnetic Reynolds number $\widetilde{Rm} = RmE^{1/3}$ represents the strength of electromagnetic induction relative to ohmic diffusion at the convective scales. Large-scale dynamos are expected to be found for $\widetilde{Rm} \lesssim O(1)$ (Yan & Calkins 2022). The distinction between large- and small-scale dynamos (Tilgner 2012) is apparent from the mean energy fraction $\langle \mathfrak{M} \rangle / M$, where $M = \langle \mathfrak{M} \rangle + \langle M \rangle$. For the small-scale dynamos, the volume-averaged MME is three orders of magnitude smaller than the TME, while they are of the same order for the large-scale dynamos. Additionally, the fraction of magnetic energy M/E , where $E = M + K$ is the total energy, can be regarded as the efficiency of the dynamo action.

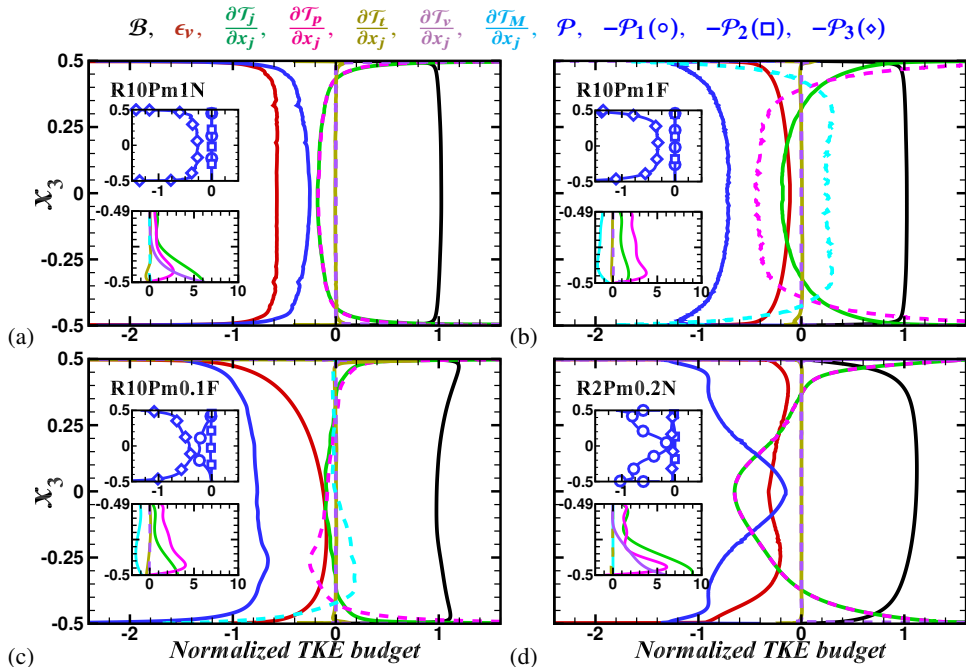


Figure 3: Vertical variation of the terms in TKE budget for (a) R10Pm1F, (b) R10Pm1N, (c) R10Pm0.1F, (d) R2Pm0.2N, cases. The insets in the top left corners show the components of the energy exchange \mathcal{P} . The insets in the bottom left corners show a breakup of the transport terms $\partial\mathcal{T}_j/\partial x_j$

3. Results

Figure 3 demonstrates the vertical variation of the horizontally averaged TKE terms in equation 2.8 for the four cases. All the terms in this equation have been averaged over time, and normalized by $(RaPr)^{1/2}/(Nu - 1)$ in the figure, so that the volume average of the source term (\mathcal{B}) is unity (Kerr 2001). The Nusselt number $Nu = qd/k\Delta T$, where q is the total vertical heat flux, is a non-dimensional measure of convective heat transport through the fluid layer, as reported in table 1. At a statistically stationary state, there is a primary balance among the turbulent buoyancy flux (\mathcal{B}), TKE transport ($\partial\mathcal{T}_j/\partial x_j$), viscous dissipation (\mathcal{D}) and the conversion to magnetic energy (\mathcal{P}) for all the dynamos. The individual components of \mathcal{P} and $\partial\mathcal{T}_j/\partial x_j$ are shown in the top and the bottom insets, respectively. For instance, in figure 3a, the TKE is generated by \mathcal{B} in the bulk, which is partly transported by $\partial\mathcal{T}_j/\partial x_j$ towards the boundaries where \mathcal{D} dominates. Among the transport components, the pressure transport ($\partial\mathcal{T}_P/\partial x_j$) is the primary mechanism that transfers TKE towards boundaries while the viscous transport is higher near the boundaries as observed in the bottom inset, similar to non-rotating non-magnetic RBC (Petschel *et al.* 2015). The vertical variation of all the terms, except \mathcal{P} , are qualitatively similar with non-magnetic rotating convection (Kunnen *et al.* 2009; Guzmán *et al.* 2020).

The small-scale dynamos R10Pm1N and R10Pm1F in figure 3a and 3b differ only in the boundary conditions. The choice of a no-slip boundary condition in R10Pm1N results in an Ekman layer near the boundaries. Moreover, the perfectly conducting magnetic boundary condition constrains the magnetic field to be horizontal near the boundaries as compared to a vertical magnetic field at the boundaries for a pseudo-vacuum boundary condition in R10Pm1F (Naskar & Pal 2022b). For both of these dynamos, the small-scale production of

case	$\langle \mathcal{P}_1 \rangle$	$-\langle \mathcal{P}_2 \rangle$	$\langle \mathcal{P}_3 \rangle$	$-\langle \mathcal{P}_6 \rangle$	$\langle \mathcal{D} \rangle$	$\langle \mathcal{D}^M \rangle$	$\langle \mathcal{D}^M \rangle$	type
R10Pm1N	0.0002	0.0000	0.3491	0.0000	0.6232	0.3507	0.0000	small
R10Pm1F	0.0004	0.0014	0.7549	0.0013	0.1627	0.7612	0.0001	small
R10Pm0.1F	0.1397	0.0093	0.5696	0.0069	0.2457	0.7189	0.0026	large
R2Pm0.2N	0.3399	0.0068	0.0538	-0.0055	0.6252	0.3878	0.0120	large

Table 2: Volume-averaged diagnostic quantities for the dynamo simulations at $E = 5 \times 10^{-7}$ and $Pr = 1$. The last column indicates the dynamo types.

magnetic energy (\mathcal{P}_3) is the dominant component of \mathcal{P} . For R10Pm1N, the amount of TKE converted to IE via \mathcal{D} is higher than the production of magnetic energy (\mathcal{P}), whereas the latter is higher for R10Pm1F (see also table 2). Another difference between these dynamos arises from the transport of TKE due to magnetic energy, which is dominated by the small-scale flux $\overline{u'_i B'_i B'_j}$, while the large-scale flux $\overline{B_j u'_i B'_i}$ remains small. The small-scale magnetic field transports TKE towards the interior from the boundaries in R10Pm1F, while the same term is small for R10Pm1N. The viscous transport dominates the other transport terms near the boundaries for R10Pm1N. However, this term is small near the boundaries in R10Pm1F owing to the absence of an Ekman layer.

A comparison between the small-scale dynamo R10Pm1F with the large-scale dynamo R10Pm0.1F reveals significant differences in the energy pathways. The mean magnetic field plays an important role in converting TKE to TME through the term \mathcal{P}_1 in R10Pm0.1F, while this term is insignificant for R10Pm1F. However, for both cases, the redistribution of TKE by the magnetic field plays a part in the budget with a major contribution from the small-scale flux $\overline{u'_i B'_i B'_j}$ in R10Pm1F, while the large-scale flux $\overline{B_j u'_i B'_i}$ is significant for R10Pm0.1F. Additionally, we can contrast the large-scale turbulent dynamo R10Pm0.1F against a large-scale dynamo with weakly non-linear convection R2Pm0.2N in figure 3. For R2Pm0.2N, the conversion of TKE to TME occurs through \mathcal{P}_1 while the small-scale production of TME, \mathcal{P}_3 remains small. Among these four dynamos, the part of TKE that converts to IE due to \mathcal{D} is higher, as compared with the conversion to magnetic energy via \mathcal{P} , when no-slip boundary condition is used (see table 2). The conversion to magnetic energy \mathcal{P} is higher with free-slip conditions, which makes R10Pm1F and R10Pm0.1F more efficient dynamos with higher magnetic energy fraction M/E , as compared to the no-slip boundary condition. Also, the transport of TKE by the magnetic field is significant only for pseudo-vacuum magnetic boundary conditions.

The magnetic energy balance of the dynamos is presented in figure 4. The solid lines represent the terms in the TME budget and are plotted at the bottom abscissa. The terms of the MME budget are represented by the dashed lines and are plotted at the top abscissa. The energy flow direction of each dynamo in figure 1 becomes apparent with the help of table 2 and figure 4. The terms \mathcal{P}_1 and \mathcal{P}_3 are positive, representing a conversion of TKE to TME by the action of a large-scale and a small-scale magnetic field, respectively. The term \mathcal{P}_2 is negative, indicating a generation of MME at the expense of TKE. The term \mathcal{P}_6 has negative values indicating a conversion of MME to generate TME, except for the case R2Pm0.2N where the turbulent magnetic field provides energy to the mean magnetic field, exhibiting an upscale transfer of energy.

In figure 4a the small-scale dynamo R10Pm1N has a primary balance between the small-scale production \mathcal{P}_3 and the Joule dissipation \mathcal{D}^M . In comparison to these TME terms, the MME terms are three orders of magnitude smaller. The part of TKE that converts to MME (\mathcal{P}_2) again transforms to TME, with a small mean dissipation \mathcal{D}^M . A similar energy conversion is observed in R10Pm1F in figure 4b, though the MME budget terms are one order of magnitude higher than R10Pm1N. Unlike R10Pm1N, the transport of TME $\partial \mathcal{T}_j^M / \partial x_j$

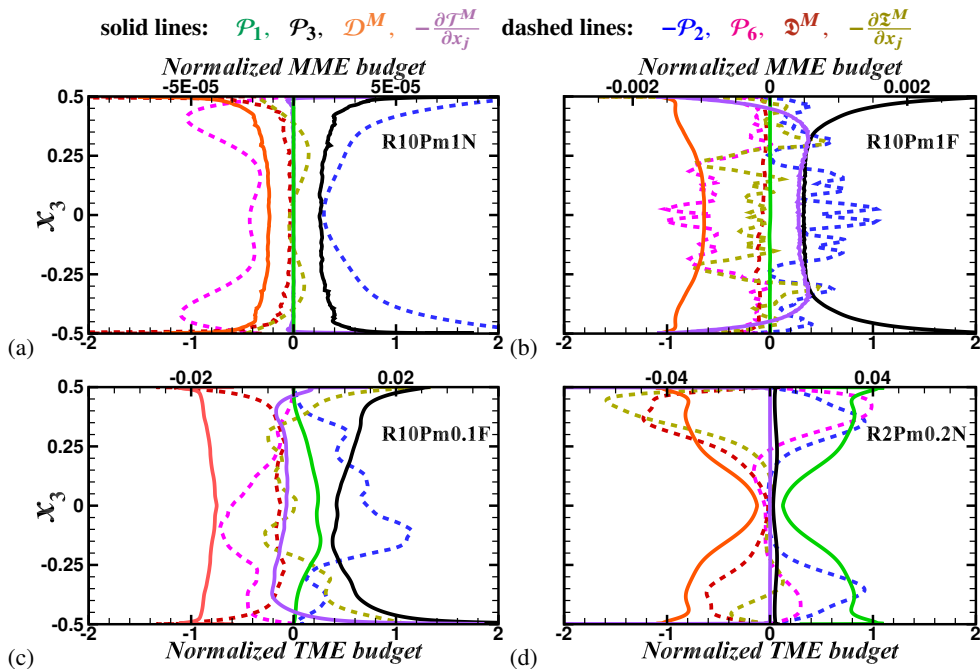


Figure 4: Vertical variation of the terms in TME and MME budgets for (a) R10Pm1F, (b) R10Pm1N, (c) R10Pm0.1F, (d) R2Pm0.2N cases. TME(MME) budget terms are plotted using solid(dotted) lines and are to be read from the bottom(top) abscissa.

plays a significant role in the balance in R10Pm1F by redistributing the TME from the boundaries towards the interior of the domain. For the large-scale dynamos R10Pm0.1 in figure 4c, the MME terms increase by another order of magnitude compared to the small-scale dynamo R10Pm1F. Further, the large-scale production of TME term \mathcal{P}_1 now makes a significant contribution to the budget in the interior of the domain. In the MME budget, \mathcal{P}_2 is partially balanced by \mathcal{P}_6 in the interior. However, the rest of the MME is transported towards the boundary and converted to IE by Joule dissipation \mathcal{D}^M . The large-scale dynamo in figure 4d demonstrates a transfer of TME to MME by \mathcal{P}_6 near the boundaries. This is the only dynamo where both the small-scale velocity and magnetic fields provide energy to the mean magnetic field through \mathcal{P}_2 and \mathcal{P}_6 . Additionally, the large-scale production \mathcal{P}_1 is the primary source of TME generation whereas \mathcal{P}_3 remains small in this case, in contrast to R10Pm0.1F in figure 4c.

4. Conclusions

In summary, we have performed direct numerical simulations of four dynamos to compare their magnetic and kinetic energy budgets. The small-scale dynamos R10Pm1N and R10Pm1F differ by the relative magnitude of small-scale magnetic energy production \mathcal{P}_3 and viscous dissipation \mathcal{D} , with the latter being higher for R10Pm1N. This indicates comparatively efficient dynamo action with free-slip, pseudo-vacuum boundaries that also promote the redistribution of TKE by the magnetic field, unlike a dynamo with no-slip, perfectly conducting boundaries. Nevertheless, the mean Joule dissipation is small for small-scale dynamos. The mechanism for transforming TKE to TME differs between a large- and a small-scale turbulent dynamo, with the large-scale production of TME \mathcal{P}_1 playing a significant role in the former. This large-scale production \mathcal{P}_1 becomes the dominant

mechanism of TME production in the weakly non-linear dynamo R2Pm0.2N. MME is produced from TKE via the term \mathcal{P}_2 in the presence of a mean magnetic field gradient. For R2Pm0.2N, an upscale transfer of energy occurs through \mathcal{P}_6 , which produces MME at the expense of TME. The scaling of these energy budget terms in the limit of small viscous and inertial forces, following (Calkins *et al.* 2015), should provide valuable insights into the mechanism of energy conversion in astrophysical dynamos. Additionally, a shell-to-shell energy transfer analysis (Guzmán *et al.* 2020) may elucidate further details on the mechanism of large-scale magnetic field generation.

Declaration of interests. The authors report no conflict of interest.

Author contributions. The authors contributed equally to analyzing data and reaching conclusions, and in writing the paper.

REFERENCES

- BRANDENBURG, A., JENNINGS, R. L., NORDLUND, Å, RIEUTORD, M., STEIN, R.F. & TUOMINEN, I. 1996 Magnetic structures in a dynamo simulation. *J. Fluid Mech.* **306**, 325–352.
- BRANDENBURG, A. & SUBRAMANIAN, K. 2005 Astrophysical magnetic fields and nonlinear dynamo theory. *Phys. Rep.* **417** (1-4), 1–209.
- CALKINS, M.A., JULIEN, K., TOBIAS, S.M. & AURNOU, J.M. 2015 A multiscale dynamo model driven by quasi-geostrophic convection. *J. Fluid Mech.* **780**, 143–166.
- CHILDRESS, S. & SOWARD, A. M. 1972 Convection-driven hydromagnetic dynamo. *Phys. Rev. Lett.* **29** (13), 837.
- GAYEN, B., HUGHES, G. O. & GRIFFITHS, R. W. 2013 Completing the mechanical energy pathways in turbulent rayleigh-bénard convection. *Phys. Rev. Lett.* **111** (12), 124301.
- GUZMÁN, A. J. A., MADONIA, M., CHENG, J. S., OSTILLA-MÓNICO, R., CLERCX, H. J. H. & KUNNEN, R. P. J. 2020 Competition between ekman plumes and vortex condensates in rapidly rotating thermal convection. *Phys. Rev. Lett.* **125** (21), 214501.
- KERR, R.M. 2001 Energy budget in Rayleigh–Bénard convection. *Phys. Rev. Lett.* **87**, 244502–1–244502–4.
- KUNNEN, R.P.J., GEURTS, B.J. & CLERCX, H.J.H. 2009 Turbulence statistics and energy budget in rotating Rayleigh–Bénard convection. *Eur. J. Mech. B Fluids* **28** (4), 578–589.
- LUMLEY, L.J. & TENNEKES, H. 1997 *A First course in turbulence*. The MIT Press.
- NASKAR, S. & PAL, A. 2022a Direct numerical simulations of optimal thermal convection in rotating plane layer dynamos. *J. Fluid Mech.* **942**, A37.
- NASKAR, S. & PAL, A. 2022b Effects of kinematic and magnetic boundary conditions on the dynamics of convection-driven plane layer dynamos. *J. Fluid Mech.* **951**, A7.
- PAL, ANIKESH 2020 Deep learning emulation of subgrid-scale processes in turbulent shear flows. *Geophys. Res. Lett.* **47** (12), e2020GL087005.
- PAL, A. & CHALAMALLA, V.K. 2020 Evolution of plumes and turbulent dynamics in deep-ocean convection. *J. Fluid Mech.* **889**, A35.
- PAL, A. & SARKAR, S. 2015 Effect of external turbulence on the evolution of a wake in stratified and unstratified environments. *J. Fluid Mech.* **772**, 361–385.
- PAL, A., DE STADLER M.B. & S., SARKAR 2013 The spatial evolution of fluctuations in a self-propelled wake compared to a patch of turbulence. *Phys. Fluids* **25**, 095106.
- PETSCHER, K., STELLMACH, S., WILCZEK, M., LÜLFF, J. & HANSEN, U. 2015 Kinetic energy transport in Rayleigh–Bénard convection. *J. Fluid Mech.* **773**, 395–417.
- STELLMACH, S. & HANSEN, U. 2004 Cartesian convection driven dynamos at low Ekman number. *Phys. Rev. E.* **70** (5), 056312.
- TILGNER, A. 2012 Transitions in rapidly rotating convection driven dynamos. *Phys. Rev. Lett.* **109** (24), 248501.
- YAN, M. & CALKINS, M. A. 2022 Strong large scale magnetic fields in rotating convection-driven dynamos: The important role of magnetic diffusion. *Phys. Rev. Res.* **4** (1), L012026.